Geophysical Journal International

*Geophys. J. Int.* (2011) **186,** 401–417 doi: 10.1111/j.1365-246X.2011.05059.x

# Characterization of pulverized granitoids in a shallow core along the San Andreas Fault, Littlerock, CA

Neta Wechsler,[1,2,*] Emily E. Allen,[2] Thomas K. Rockwell,[2] Gary Girty,[2] Judith S. Chester[3] and Yehuda Ben-Zion[1]

[1]*Department of Earth Sciences, University of Southern California, Los Angeles, CA 90089, USA. E-mail: wechsler@ipgp.fr*
[2]*Department of Geological Sciences, San Diego State University, San Diego, CA 92182, USA*
[3]*Department of Geology and Geophysics, Texas A&M University, College Station, TX 77843, USA*

Accepted 2011 April 27. Received 2011 April 25; in original form 2010 November 21

## SUMMARY

We present results on the composition, structure and particle size distribution (PSD) of pulverized and damaged granitic rocks in a 42-m-deep core adjacent to the San Andreas Fault near Littlerock, CA. The cored section is composed of pulverized granites and granodiorites, and is cut by numerous mesoscopic secondary shears. The analysis employs XRD, XRF, thin sections and semi-automated particle size analyser methods, including a novel calibration method. The mean particle size for the majority of samples falls between 50 and 470 $\mu$m. The PSDs can be fitted by a power law, with $D$-values ranging between 2.5 and 3.1, as well as by a superposition of two Gaussians. Fracture surface energy calculations based on the observed particle distributions provide very low values, indicating that the part of the total earthquake energy budget expended for breaking or shattering rocks is small. Shear deformation is likely to dominate near secondary faults. The most pronounced fault-related alteration occurs along the secondary shears, and is a function of both composition and depth. The alteration to clay appears to be the result of fluid–rock interaction and brittle deformation under low temperature conditions, rather than of surface-related weathering. The particle size reduction noted in the core reflects multiple mechanisms of comminution. The zones of pulverization that lack significant weathering likely result from repeating episodes of dynamic dilation and contraction.

**Key words:** Geomechanics; Microstructures; Fault zone rheology; Dynamics and mechanics of faulting; Fractures and faults.

## 1 INTRODUCTION

Highly fractured rock (referred to as rock flour, rock powder, breccia and pulverized rock) has long been recognized along surface traces of the San Andreas and other strike-slip faults (e.g. Flinn 1977; Anderson *et al.* 1980, 1983). In the framework of the standard fault zone model (e.g. Sibson 1986; Chester *et al*. 1993), this highly fractured rock occurs outside of the fault-core, in the surrounding damage zone, and is distinct from gouge or cataclasite, which result from shear within the fault-core. Primarily, the highly fractured rock has been described as having a powdery texture in outcrop, reflecting deformation at the microscopic scale dominated by Mode I (opening) fractures that display little or no shear displacement (e.g. Dor *et al.* 2006). Recently, this fault-associated rock (henceforth referred to as 'pulverized') has received considerable attention, as it is recognized as a fundamental characteristic of the damage zone along the San Andreas Fault (SAF), particularly for granite bodies (Wilson *et al.* 2005; Dor *et al.* 2006). Pulverized granite (PG) has also been documented recently along portions of the Garlock Fault (Rockwell *et al.* 2009), the San Jacinto Fault (Stillings 2007) and the Arima-Takatsuki tectonic line in Japan (Mitchell *et al.* 2011). Some of these studies have analysed the details of PG chemistry and its physical properties.

Pulverization is thought to be associated with dynamic reduction of normal stress during earthquake ruptures (Brune *et al.* 1993; Ben-Zion & Shi 2005; Wilson *et al.* 2005), which is expected to be enhanced (e.g. Ben-Zion & Andrews 1998; Shi and Ben-Zion 2006; Brietzke *et al*. 2009) for ruptures on a bimaterial interface. Doan & Gary (2009) demonstrated with laboratory experiments that pulverization requires high strain rates, and suggested that observed pulverized rocks may have been produced by supershear ruptures. However, it is generally accepted that earthquake rupture speeds are typically about 75 per cent of the shear wave velocity (e.g. Ben-Zion 2003). This is consistent with theoretical understanding that supershear ruptures require more stringent conditions (higher and more uniform initial shear stress) than those needed for subshear ruptures (e.g. Zheng & Rice 1998). High coseismic strain rates in

*Now at: Laboratoire de Tectonique, Institut de Physique du Globe de Paris, 75252 Paris, France.

a zone around the fault may be produced by bimaterial ruptures, which tend to be associated with slip rates of tens of metres per second (e.g. Ben-Zion 2001; Ben-Zion & Huang 2002; Dalguer & Day 2009). Supershear ruptures subject the rocks to abrupt shock-like loading that is likely to produce very small grain sizes, down to the nanoscale (Sammis & Ben-Zion 2008).

The nature of pulverized rocks along the Mojave section of the SAF has attracted attention since Brune (2001) argued that highly fractured crystalline rocks in several locations along the fault lack evidence of fault parallel shear. Dor *et al*. (2006) defined rocks from the damage zone of the SAF near Tejon pass and along the Mojave segment as 'pulverized' to indicate lack of macroscopic shear deformation. To determine the distribution of similarly pulverized rock along the Mojave section of the fault, Dor *et al*. (2006) systematically mapped the distribution and intensity of pulverized crystalline rock. They found that almost all the crystalline rocks within 50–200 m from the SAF are pulverized to varying degrees, occupying an approximately 100–200 m wide subvertical tabular zone parallel to the fault (Dor *et al.* 2006). Rockwell *et al*. (2009) and Stillings (2007) studied PG along portions of the Garlock and San Jacinto faults, respectively, and demonstrated that the pulverization is spatially related to the normal distance from the fault. Those previous studies all focused on surface and near-surface exposures (up to 2 m depth). Consequently, there is debate as to the role of surface weathering and other surficial effects in the development of PG along faults, and the depth range of pulverization.

Wilson *et al*. (2005) found little evidence of weathering in the PGs from Tejon Pass, and concluded that the pulverization reflects a mechanical process. Using measurements obtained with a laser particle analyzer they concluded that the particle size distribution (PSD) of the PG is narrow with a mean grain size in the submicron size range. Based on the inferred extreme mechanical comminution in proximity to the fault, they suggested that approximately 50 per cent of the earthquake energy budget is spent in creating new fracture surfaces in the fault zone. Their results were in contrast to previous measurements of PSDs from damaged fault zone rocks (e.g. Sammis *et al.* 1987; Chester *et al.* 2005), and related estimates that the fracture surface energy only accounts for a small fraction of the total earthquake energy budget (Chester *et al.* 2005).

Subsequent analysis of PG from the same locality studied by Wilson *et al*. (2005) and other exposures of the Tejon Lookout granites by Rockwell *et al*. (2009), demonstrated significant weathering of the $<4\ \mu$m grain size fraction. More significantly, this group found that the mean grain size (26–208 $\mu$m) at Tejon Pass and on Tejon Ranch along the Garlock Fault, is substantially coarser than that reported by Wilson *et al*. (2005), in general agreement with previous estimates of a small fraction of the earthquake energy budget going towards fracturing. Rockwell *et al*. (2009) concluded that the difference between their estimates of PSD and those of Wilson *et al*. (2005) is a result of bias originating from the measurement technique (Laser particle analyser). In this paper, we solve the measurement bias problem by introducing a new technique of instrument calibration for PSD measurements (Appendix A).

Clarifying further the properties of pulverized fault zone rocks can provide important information on the generating mechanism, *in situ* dynamic stress conditions, energy budget and other aspects of earthquake and fault mechanics. This requires systematic characterization of the composition, particle size, and deformation character of pulverized rock in the damage zones of major faults at different depth sections. In this study, we provide for the first time a detailed characterization of pulverized rocks at some depth below the surface. This is done by analysing a nearly continuous (∼95 per cent recovery), 42-m-deep, 6.35 cm diameter, oriented core of pulverized fault zone rock adjacent to the SAF near Littlerock, southeast of Palmdale (Fig. 1). The core is composed mainly of felsic igneous rocks, and crosses several secondary fault zones that contain gouge zones that are up to several centimetres thick. Our goal is to characterize the compositional variations, and the distribution and type of damage as a function of depth for the cored zone adjacent to the active trace of the SAF at Littlerock.

Below we provide a general overview of the location of the drill site, a description of the rock structure and composition, the chemical characterization of the cored interval using XRF and XRD methods, and the PSD measured using both pipette rack and laser particle analyser. We then discuss the implications of our findings in the context of the earthquake energy budget and fault zone related processes.

## 2 CORE CHARACTERIZATION

### 2.1 Geological settings

The drill site is located approximately 80 m south of the primary active trace of the SAF near Littlerock Creek, southeast of Palmdale and north of the San Gabriel Mountains (Fig. 1). At this locality, the active trace of the SAF is relatively straight, and slip is localized along the active fault. The geology in the study area was mapped by Barrows *et al*. (1985). Surface exposures of Mesozoic granitoids, which are typically overlain by Quaternary alluvial deposits, are exposed mostly on hill slopes, and extend from the main strand of the SAF towards the south (Fig. 2). About 500 m south of the SAF, the granites are overlain by the Neogene Juniper Hills Formation (JHF), an alluvial-fluvial sedimentary unit that is offset ∼20 km along the SAF. Bedding planes within the JHF are steeply tilted. Barrows *et al*. (1985) interpreted the JHF to be in fault contact with the granites. Approximately 1 km south of the SAF, the Nadeau Fault, a thrust fault that places quartz diorite over the JHF, is mapped in very close proximity to the inferred trace of the now inactive Punchbowl Fault (PF). The San Gabriel Mountains rise to the south of the Nadeau Fault, exposing extensive areas of Mesozoic granodiorite (Lowe pluton).

The granitic rock body drilled during this study could be a sliver of igneous rock sandwiched between the SAF and PF. Its surface exposure extends from about halfway between the PF and the present-day active strand of the SAF, and the PF dies out in this area. Dor *et al*. (2006) found an asymmetry of rock damage across the SAF in the Mojave, with more pulverization and damage products north of the fault, whereas the drill site is south of the fault. This location was chosen for its accessibility and because it is one of the few places along the Mojave segment of the SAF where there is a large surface exposure of granitic rocks right up to the fault.

We employed a standard soil-drilling rig (split-spoon auger) and recovered a continuous, 6.35 cm diameter core to a depth of about 35 m during the first day of drilling. Unfortunately, the drill seized up the following day, forcing us to abandon some of the drill stem. We then stepped over a few metres and obtained a core sample from 35 to 42 m in depth. The rocks encountered are severely pulverized, and therefore only about 40 per cent of the recovered core remained completely intact when placed in storage boxes. Additional representative surface samples were collected from an outcrop adjacent to the drill site to allow characterization of the uppermost 2 m of rock. Core sample names start with LR, followed by a number, with ascending numbers corresponding to greater depths. Surface sample names from the adjacent outcrop starts with DO, followed

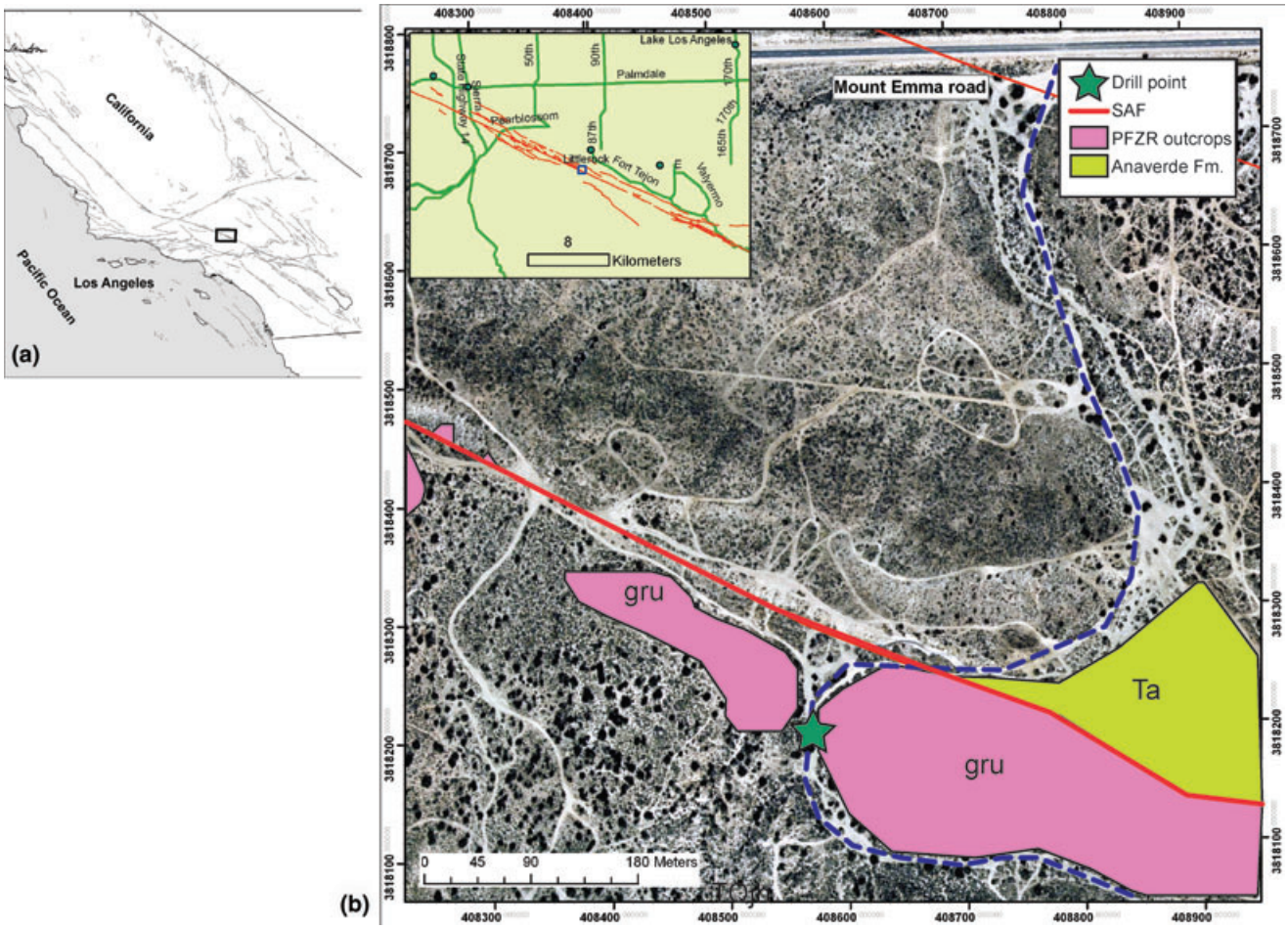


**Figure 1.** Location map of the drill site. (a) General location and major faults in southern California. (b) An air-photo of the location of the drill site (star). gru – Mesozoic granitoids. Ta – Neogene Anaverde Fm. PFZR stands for 'pulverized fault zone rocks'. Note the offset creek (dashed blue line).

by a number. We also collected several additional non-pulverized surface samples from an outcrop approximately 500 m away from the SAF. Those samples are assumed to represent the non-damaged protolith outside the fault's damage zone, and will be referred to henceforth as 'protolith'.

### 2.2 Lithology and structure

The orientation of the core is known to within $\pm 10^{\circ}$. The core captured three primary rock types, and crossed several secondary shear zones and localized faults, consisting of narrow zones of dark, clayey, dense fault gouge. In general, the core is composed of about 40 per cent granite, 45 per cent granodiorite and 15 per cent quartz diorite, the latter rock type appearing only in the deepest part of the core. A detailed log of the core is presented in Figs S1–S3 and the mineralogy of the three primary rock types is presented in Table 1.

Granite samples are white to pink in colour, generally lack mafic minerals, and are very friable in character. They are composed mostly of quartz, K-feldspar and plagioclase (mostly albite), with muscovite and little or no biotite. The K-spars exhibit perthitic textures. Some of the quartz grains display undulatory extinction and deformation band development. Calcite is rarely present in veins. The muscovite is characterized by chlorite and opaque iron oxide along seams parallel to $\{001\}$. In thin section garnet, zircon and apatite are apparent. All grains regardless of mineral type are fractured to various degrees. Plagioclase-feldspar grains tend to break along cleavage planes, but not exclusively so (Fig. 3a). Plagioclase grains are often altered to sericite.

Granodiorite samples are composed of quartz, plagioclase (albite-oligoclase), K-feldspar, biotite and minor amounts of chlorite, epidote, titanite, calcite and iron oxides. The granodiorite samples containing chlorite are usually more intact than the granites. The calcite and iron oxide appear as cement in cataclastic zones. Calcite also grows in cracks and voids and is twinned and fractured (Figs 3b and c). Biotite is oftentimes replaced by chlorite, and some plagioclase grains are often altered to sericite or laumontite (Fig. 3d). Some of the quartz grains display undulatory extinction and deformation band development. All grains regardless of mineral type are fractured to various degrees.

Quartz diorite appears only in the bottom of the cored interval. These rocks are mostly greenish-brown, and are more altered and fractured into clay size ($<2\ \mu$m) fragments. The diorites are composed of mostly chlorite, quartz, plagioclase, biotite, iron oxides, titanite and minor amounts of calcite. Various stages of chlorite replacement of biotite are evident in thin section (Fig. 3e). In addition, clear, translucent, pore-filling authigenic chlorite is present in some specimens.

Numerous sections of the core are cut by centimetre to several centimetre thick shears or secondary faults. The thinnest shears observed in hand samples are about 1 mm thick, and are filled with greyish or greenish clay size grains (Fig. 3f). The orientations of the shears and secondary faults were recorded where possible

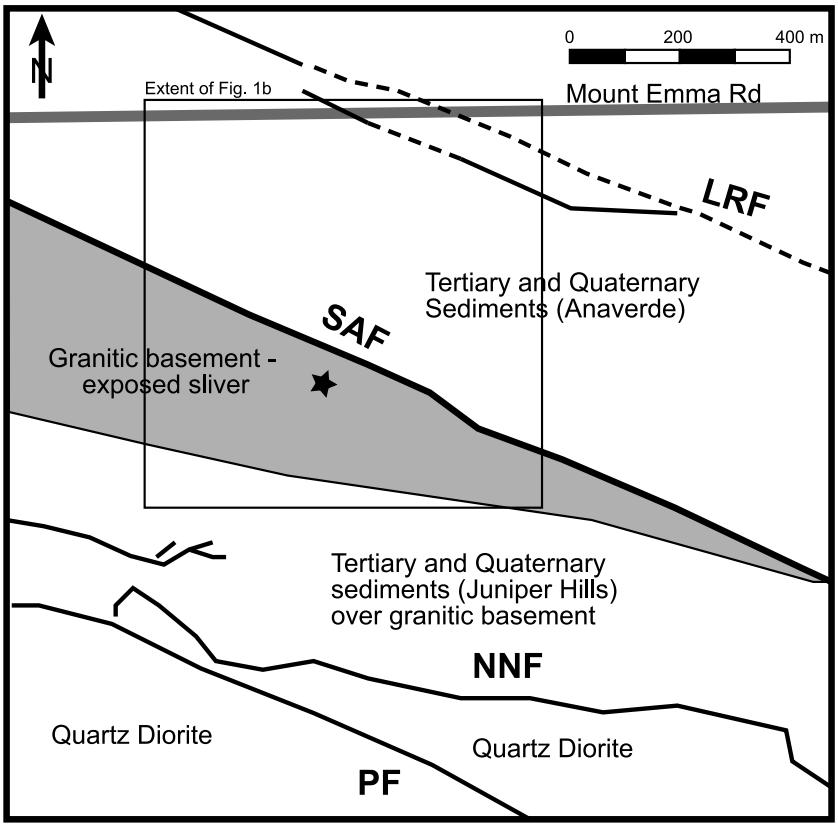


**Figure 2.** A simplified geological map of the study area modified from Barrows *et al*. (1985). Major units and faults are marked. SAF, San Andreas Fault; LRF, Littlerock Fault; NNF, Northern Nadeau Fault; PF, Punchbowl Fault. Drill site location is marked with a star.

(Figs S1 and S2), but no systematic orientation distribution was established. The suggested random fabric may partially reflect the uncertainty in core orientation. The overall damaged nature of the cored interval made it difficult to determine unequivocally the origin of the mesoscale open fractures.

Towards the bottom of the core there are several gouge zones of varying thickness, composed of dark brown to black, highly cohesive clay. Some of these zones contain small (up to 2–3 mm in diameter) fragments of the surrounding rock. The widest gouge zone occurs at 36.5 m depth and is about 30 cm thick. These gouge zones are interpreted to represent significant secondary faults within the SAF zone.

## 3 PARTICLE SIZE DISTRIBUTION

### 3.1 Methods

Multiple splits of samples from the core and two analysis methods were used to determine PSD (see Appendix A for an extended description of the methods).

As noted by Rockwell *et al*. (2009), laser particle size analysers do not necessarily give the same results as the pipette-sieve method, either because of sedimentation in the machine, or because of the internal algorithms that convert the diffraction data to PSD, or a combination of both. Therefore, to ensure accurate and reproducible results, we used a standard pipette and dry sieve method (Rockwell 2000; Rockwell *et al.* 2009) in conjunction with light-microscopy particle analysis to calibrate the automated analyses performed with a laser particle size analyser (Horiba LA-930 laser diffraction particle size analyser) combined with a camsizer (Retsch particle size analyser). Sample preparation followed that described by Rockwell *et al*. (2009) with one exception: for the automated method, samples were wet sieved at 125 $\mu$m instead of 63 $\mu$m to produce more consistent results.

Using the standard samples to calibrate the Horiba analyser, entire splits were measured using the methods described in Appendix A. The Horiba analyser and camsizer results are then combined by weight per cent (Fig. 4). Comparing the classical versus automated method, it was found that in most samples, the classical method seemed to slightly underestimate the amount of fine material compared with the automated method (Fig. 4), which we attribute to the much finer lower detection limit of the Horiba analyser (0.2 $\mu$m) compared with the standard pipette method (1–2 $\mu$m).

### 3.2 Results

The PSD of PG is mostly fine sand and silt in size. The mean particle size for the majority of samples falls between 50 and 470 $\mu$m (Fig. 5), much coarser than originally proposed by Wilson *et al*. (2005). There is a slight fining of PSD with depth, but no apparent correlation with rock composition. As expected, the smallest values of PSD were obtained for samples taken from sheared and gouge zones. Various fractions from the sieving process (between 31 and 500 $\mu$m) were examined under the microscope to determine if a compositional difference exists between size fractions (i.e. is there a dominating mineral in certain fractions that is lacking in others) but no significant difference was found.

We convert the volumetric PSD into linear density and plot (Fig. 6a) the log of the number of particles versus the log of their diameter to obtain the *D*-value (slope of the distribution on a log–log plot, or exponent of the power-law function) of each sample

**Table 1.** Point counts of core thin sections from various depths, which are representative of the three key rock types recovered from the core. Upper value is number of counts, lower value (in italics) is in per cent. Core samples taken for thin sectioning do not always directly correspond to samples used for geochemistry. Those sample names represent the depth they were taken from (in feet and inches). For the samples relative location in the core, see Figs S1 and S2.

| Sample name | LR023 | 0308S | 0468S | 1168D | 1219S | 1225S | 1251S | 1312S |
|---|---|---|---|---|---|---|---|---|
| Depth (m) | 9.1 | 9.3 | 14.2 | 35.4 | 36.9 | 37.1 | 38.1 | 39.7 |
| Quartz | 75 | 49 | 41 | 87 | 25 | 47 | 9 | 25 |
| | *25.0* | *16.3* | *13.7* | *29.0* | *8.3* | *15.7* | *3.0* | *8.3* |
| Plagioclase | 138 | 74 | 124 | 133 | 27 | 60 | 45 | 111 |
| | *46.0* | *24.7* | *41.3* | *44.3* | *9.0* | *20.0* | *15.0* | *37.0* |
| k-spar | 35 | 118 | 29 | 23 | 77 | 116 | 95 | 15 |
| | *11.7* | *39.3* | *9.7* | *7.7* | *25.7* | *38.7* | *31.7* | *5.0* |
| Clays[a] | 28 | 55 | 56 | 24 | 130 | 68 | 113 | 36 |
| | *9.3* | *18.3* | *18.7* | *8.0* | *43.3* | *22.7* | *37.7* | *12.0* |
| Opaques | – | 1 | 9 | 7 | 2 | – | 3 | – |
| | | *0.3* | *3.0* | *2.3* | *0.7* | | *1.0* | |
| Chlorite | 10 | – | 13 | 11 | 19 | 1 | 21 | 32 |
| | *3.3* | | *4.3* | *3.7* | *6.3* | *0.3* | *7.0* | *10.7* |
| Calcite | 1 | – | 5 | 3 | 3 | 8 | – | 11 |
| | *0.3* | | *1.7* | *1.0* | *1.0* | *2.7* | | *3.7* |
| Biotite | – | – | 18 | 12 | 2 | – | – | 36 |
| | | | *6.0* | *4.0* | *0.7* | | | *12.0* |
| Epidote | – | 1 | – | – | 15 | – | 14 | 3 |
| | | *0.3* | | | *5.0* | | *4.7* | *1.0* |
| White mica | 12 | 2 | 1 | – | – | – | – | – |
| | *4.0* | *0.7* | *0.3* | | | | | |
| Garnet | 1 | – | 3 | – | – | – | – | – |
| | *0.3* | | *1.0* | | | | | |
| Amphibole | – | – | – | – | – | – | – | 30 |
| | | | | | | | | *10.0* |
| Unknown | – | – | 1 | – | – | – | – | 1 |
| | | | *0.3* | | | | | *0.3* |
| Perthite | 13 | 38 | 2 | – | – | – | 1 | −6[b] |
| IUGS def | grano-diorite | granite | grano-diorite | grano-diorite | quartz syenite[c] | granite | quartz syenite[c] | quartz monzo-diorite |
| Matching core sample no. | LR023 | LR024 | LR035 | LR072 | none | LR074 | LR075 | LR083 |

[a]Including minerals too small for identification.
[b]Negative value for anti-perthite.
[c]More than 35 per cent clays, rock definition possibly inaccurate.

(Sammis *et al.* 1987; Blenkinsop 1991; Rockwell *et al.* 2009). For consistency, we use the same range for all samples (0.5–500 $\mu$m) and calculate their *D*-values (Fig. 6). The *D*-values correlate with the mean particle size over the range of 20–500 $\mu$m on a log-linear plot (Fig. 6b), and span the range of 2.5–3.1 with no apparent correlation to rock type.

It is possible to estimate the amount of new surface created by the pulverization of the rocks, using the same approach as Keulen *et al*. (2007). Within the core, the damage is heterogeneous, varying over length scales of less than a metre with depth. By combining all measurements from the entire core we can provide a representative, average value of fracture surface area at 80 m from the SAF at Littlerock. The fracture surface area is estimated by using the calculated minimum and maximum *D*-values in the core, the smallest grains observed in SEM as a lower bound ($d_{\min} = 0.02$ $\mu$m), and $d_{\max} =$ 4500 $\mu$m as upper bound. We set up a histogram of bins similar to the PSD measurements histogram, and for each bin calculate the number, total volume and total surface of the particles. Based on this procedure we calculate a fracture surface area of $2.06 \times 10^8$ and $2.18 \times 10^8$ m$^2$ per cubic metre of pulverized material for the minimum and maximum *D*-values, respectively. The obtained fracture surface area is 2 orders of magnitude larger than the estimate made

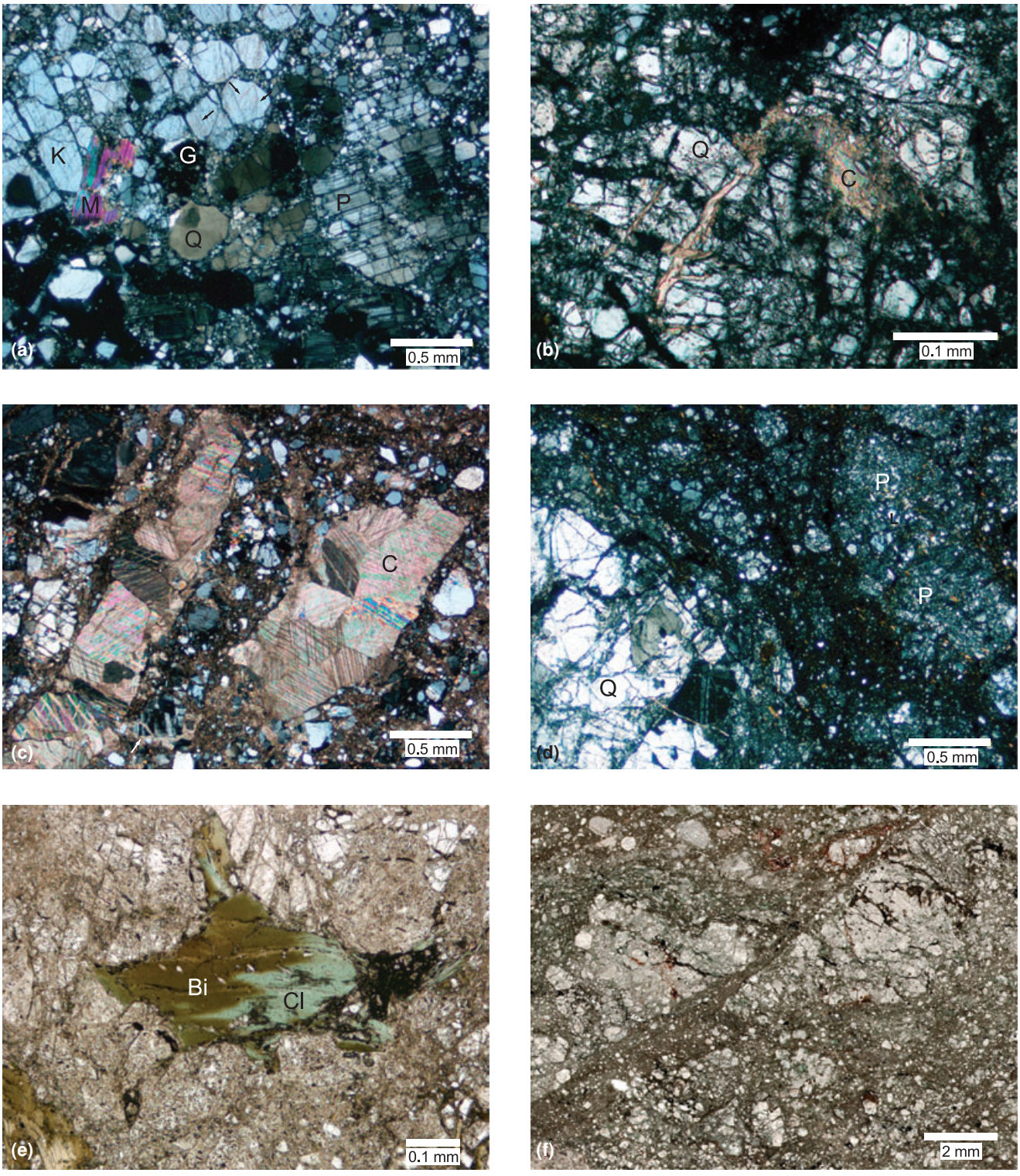


**Figure 3.** Photomicrographs of core samples. (a) Pulverization in various minerals. Plagioclase feldspar (P) breaks along cleavage (right side). Muscovite (M) seems intact (sample depth – 9.3 m). Potassium-feldspar (K) has evidence of multiple breaking and healing episodes (several examples are marked with small arrows). (b) Authigenic calcite in pulverized quartz. Two phases of calcite growth can be seen (sample depth – 14.2 m). (c) Authigenic calcite growth and twinning in cracks and voids. A zone of pulverization with calcite-filled cracks is seen on the left. A cataclastic zone with broken particles in calcite matrix is seen on the right and in between the two large calcite-filled voids. Some of the particles (for example, a feldspar and calcite grain on the bottom left, marked by an arrow) seem to have been cemented by calcite and then re-broken and cemented again, based on the difference in calcite crystal size (sample depth – 37.1 m). (d) Laumontite and sericite in plagioclase and cataclastic shears. The sericite is seen as the yellow fine grains within the plagioclase. Pulverized quartz on the left side (sample depth – 38.2 m). (e) Biotite altered into Chlorite (sample depth – 14.2 m). (f) Clay-filled shear zone, crossing the image from lower left to upper right (sample depth – 38.2 m). Q-quartz, K-potassium feldspar, P-plagioclase, G-garnet, M-muscovite, C-calcite, B-biotite, Cl- Chlorite. Images a–d were shot under cross-polarized light, and images e–f were shot under plane-polarized light.

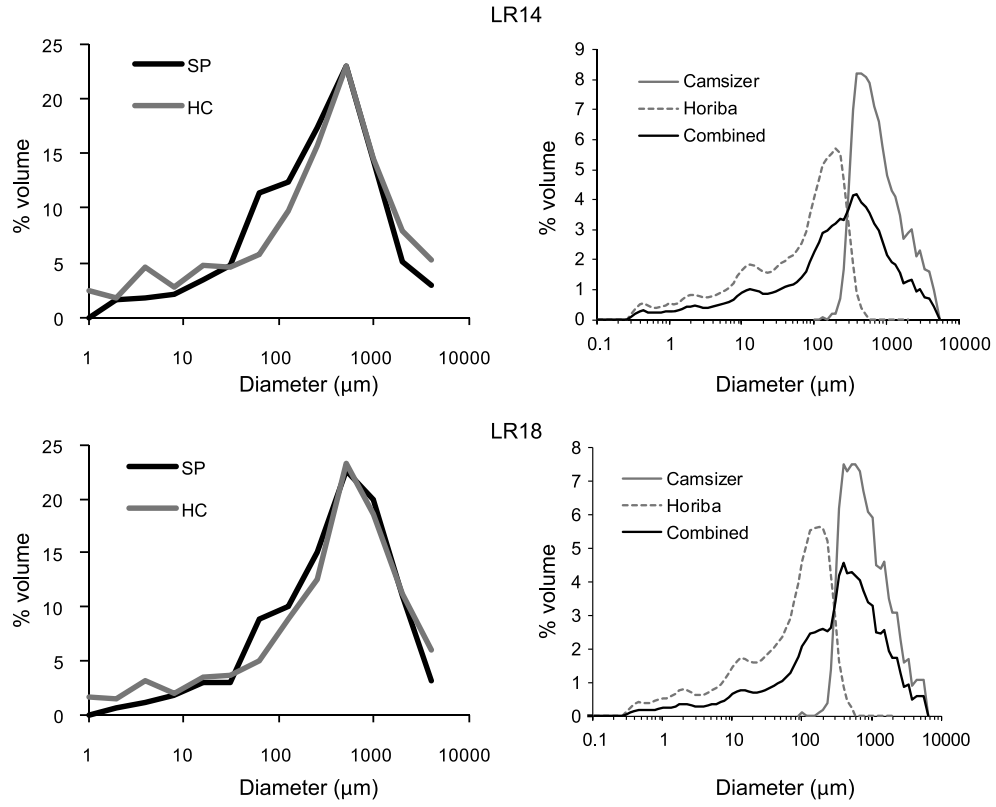


**Figure 4.** A comparison of the PSD from the classical sieve-pipette method (SP) and the automated Horiba-Camsizer (HC) measurement (rebinned to the same bins used in the classical method) for two samples – LR14, a granodiorite from 5.7 m, and LR18, a granite from 7.4 m. On the left is the classical method PSD compared to the rebinned PSD from the automated method. On the right is the original PSD from the automated method, which is the weighted sum of the measurements from the Horiba analyser and the Camsizer.

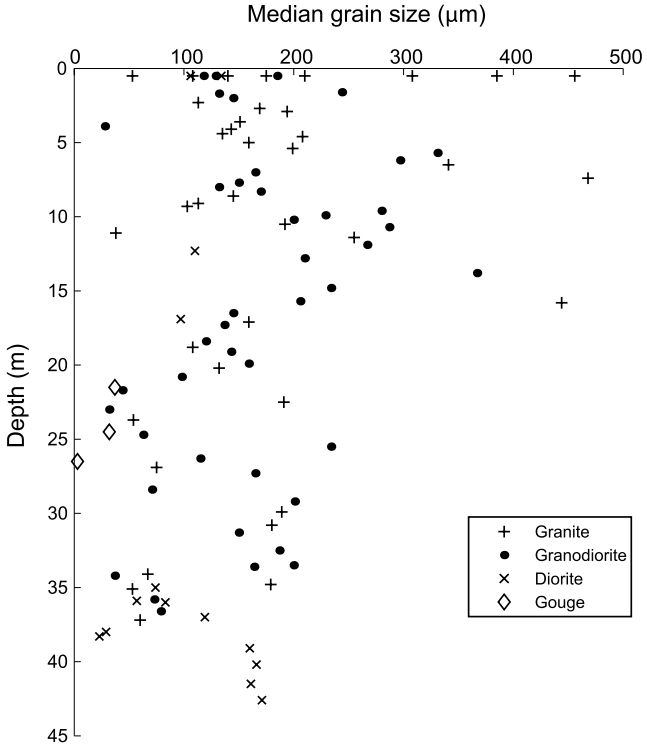


**Figure 5.** Median particle size versus depth, according to rock type. The coarsest samples appear at shallow depths of up to 15 m. Gouge samples have the finest particle size, as expected.

by Keulen *et al*. (2007), who calculated $1.3 \times 10^6$ and $6.0 \times 10^6$ m$^2$ per cubic metre for cracked material and gouge, respectively.

## 4 GEOCHEMISTRY

### 4.1 Methods

A Phillips MajiX Pro spectrometer and accompanying software were used to determine major and trace element concentrations for all samples following the method described by Girty *et al*. (2006, 2008) and used by Rockwell *et al*. (2009). The samples were first powdered in a Spex Certiprep tungsten carbide shatter box. Fused disks were used for major elemental concentrations, and pressed pellets were used for trace element concentrations. Loss on Ignition (LOI), the sum of volatile components, was also determined (Table S1).

Using the aliquot of the finest ($<2$ $\mu$m) material from our PSD samples, an XRD analysis was performed for a subset of 62 samples using a Phillips X'pert multipurpose diffractometer with copper K$\alpha$ radiation at 1.5405 Å, and 45 KV and 40 mA settings. Each sample was measured four times: untreated, glycolated, heated to 350 ˚C and heated to 550 ˚C. Typical scans were from 2˚ to 55˚ 2$\theta$ for untreated samples, and 2˚ to 20˚ 2$\theta$ for glycolated and heat-treated specimens.

### 4.2 Results

#### *4.2.1 XRF Elemental Analysis*

The three main rock types, as defined using hand samples from the core, have distinct bulk rock chemistries (Fig. 7 and Table S1).

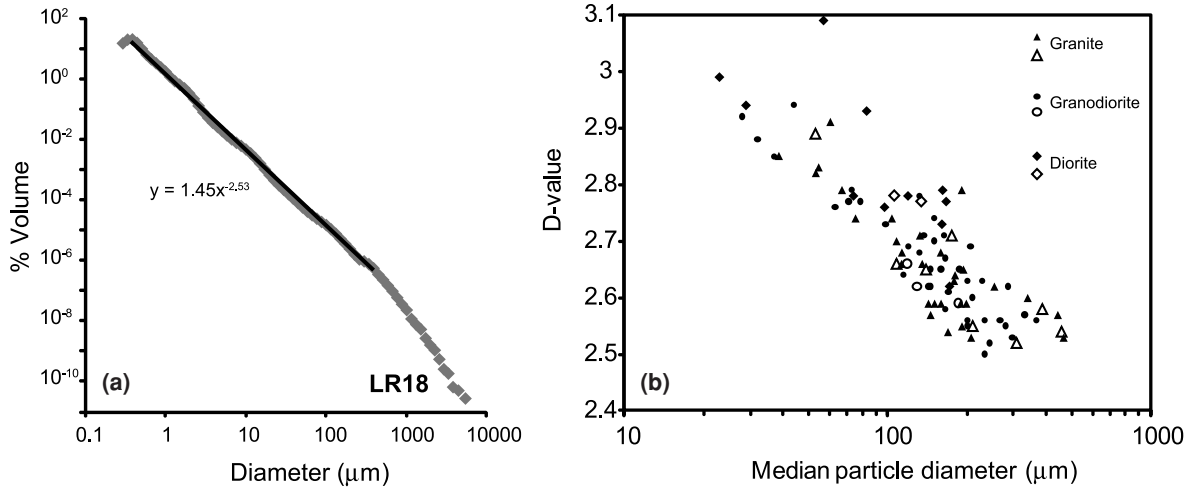


**Figure 6.** (a) An example of D-value calculation for sample LR18, a granite from 7.4 m. The PSD is fitted with a power-law function between 0.5 and 500 $\mu$m, and its exponent is recorded as the *D*-value for the sample. (b) *D*-value versus median particle size for core (filled symbols) and surface (open symbols) samples.

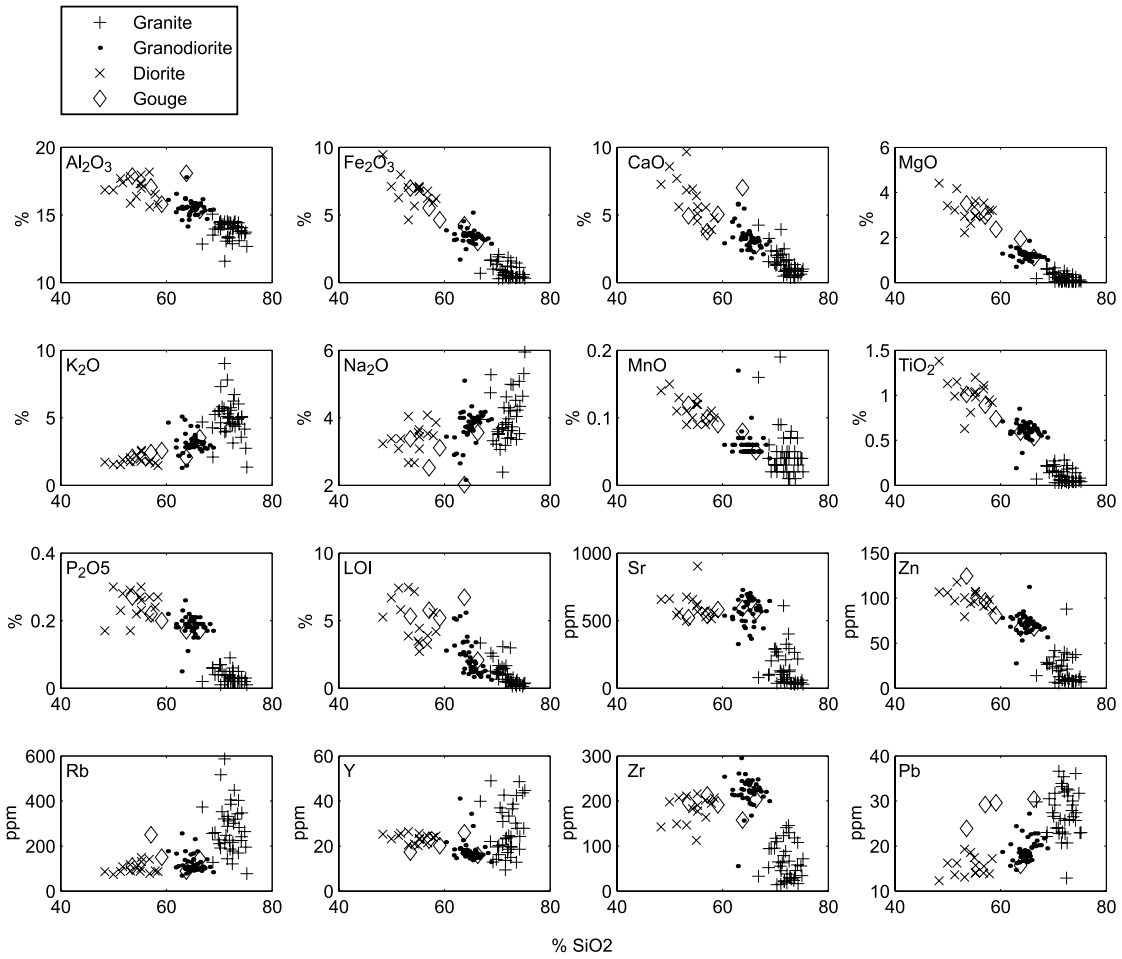


**Figure 7.** Silica variation diagrams of selected major and trace elements.

Variation in composition is almost non-existent, except at specific depths that correspond with the location of secondary faults (Fig. 8).

In order to determine the influence of secondary fault zones on sample chemistry, several host rock samples taken about 500 m from the fault zone, assumingly representing the undamaged protolith, were analysed for comparison. The protolith samples showed only minor changes in bulk rock composition compared with the fault zone samples, particularly the granodiorite samples. Compared with the granite protolith, granitic core samples show a slight increase in Fe, K, Ti, Ba, Y and Nb, and a strong depletion of Ca (Figs 9a and b). The composition of samples taken from several gouge

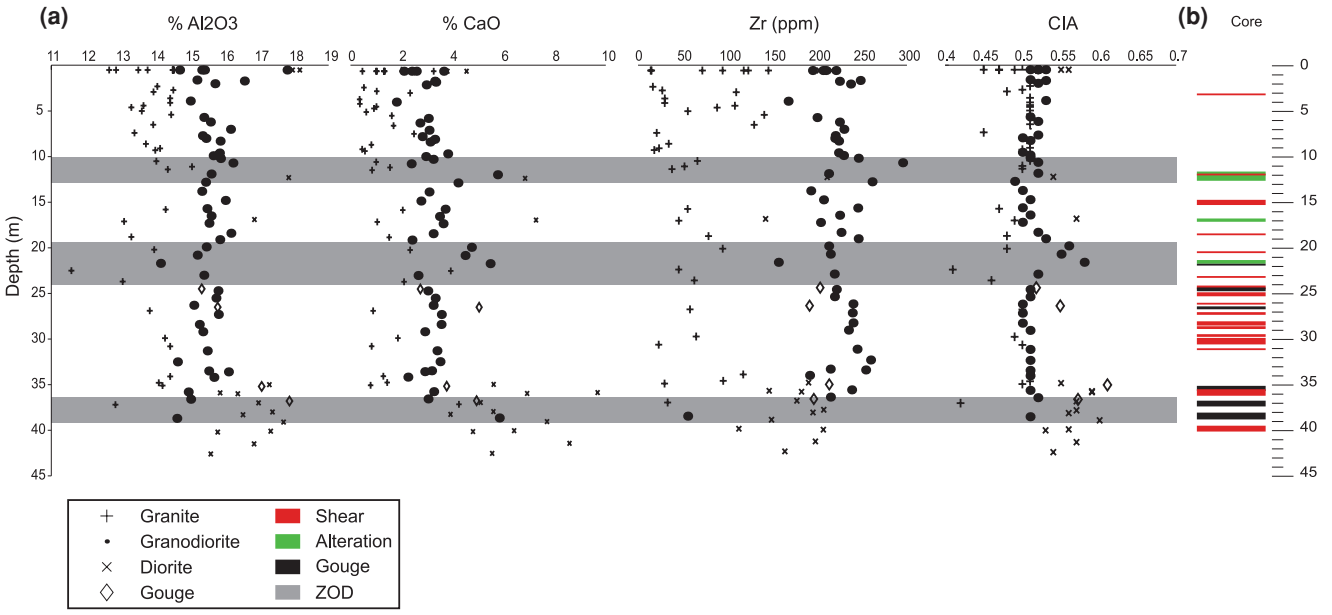


**Figure 8.** (a) Depth variation diagrams of $Al_2O_3$, CaO, Zr and CIA. Grey zones mark zones with outlier samples (ZOD). (b) Major shears and alteration bands, as well as gouge zones in the core.

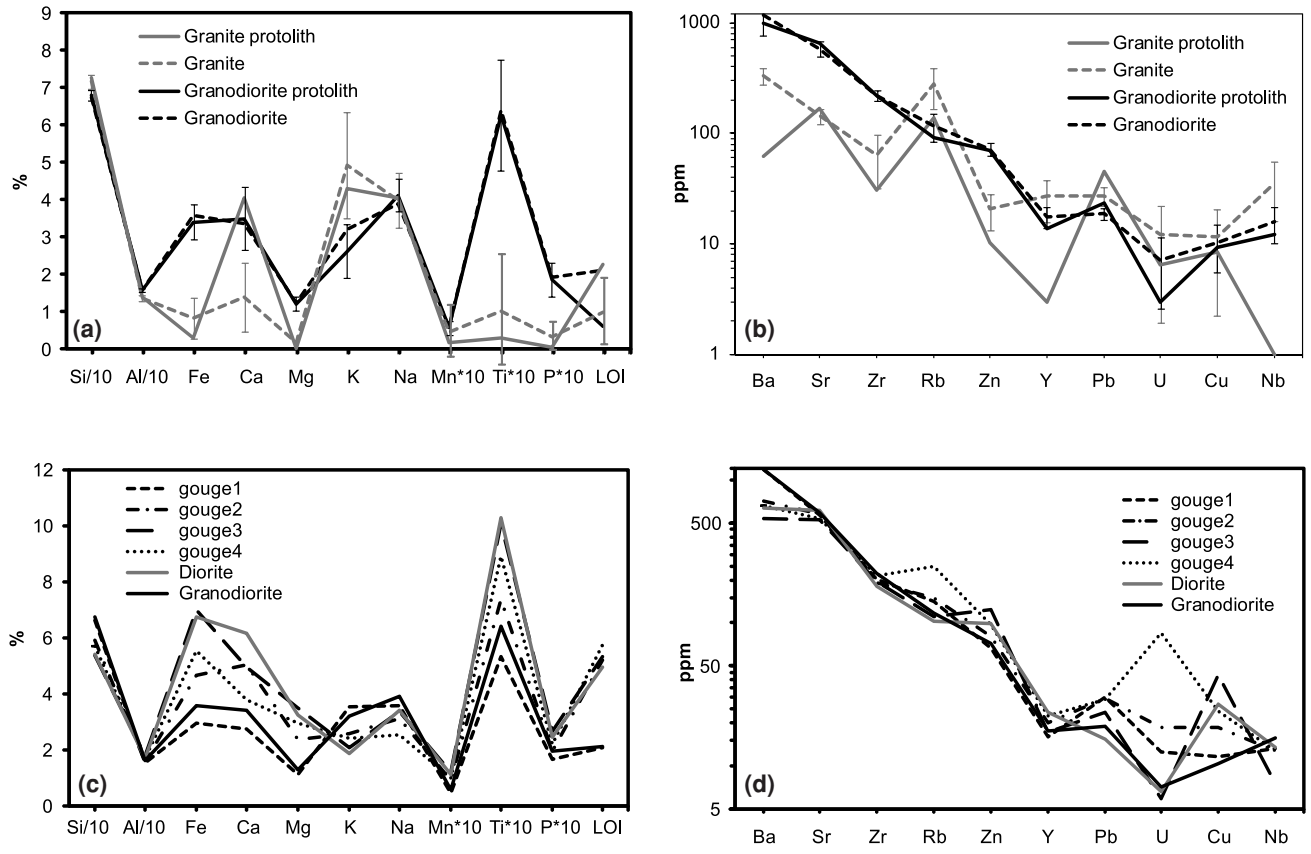


**Figure 9.** Upper – Comparisons of major (a) and trace elements (b) for core samples (averages with standard deviation error bars) and protolith (undamaged) samples. Lower – comparisons of major (c) and trace elements (d) for gouge samples and averaged granodiorite and diorite core samples.

zones falls between that of the granodiorite and the diorite in bulk rock composition (Figs 9c and d). The only deviation is in sample gouge4, where there is a relative increase in Rb and U.

We convert our major element data to molecular proportions, and calculate the chemical index of alteration (CIA) following Nesbitt & Young (1982), as follows:

$$A = Al_2O_3/(Al_2O_3 + CaO^* + N_2O + K_2O), \quad (1)$$

$$CN = (CaO^* + N_2O)/(Al_2O_3 + CaO^* + N_2O + K_2O), \quad (2)$$

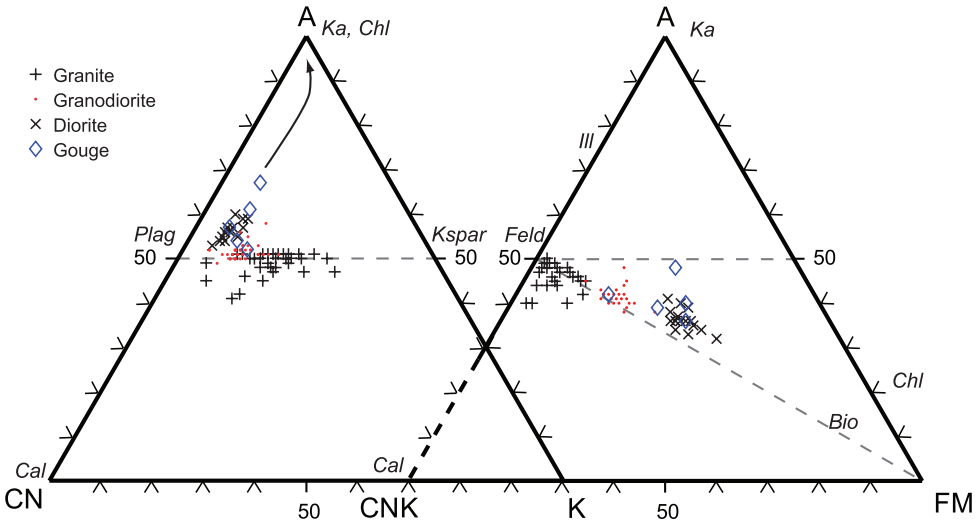


**Figure 10.** Core samples bulk compositions plotted in A-CN-K and A-CNK-FM space (see section 4.2.1 and equations 1–3 for explanation). The arrow depicts the predicted weathering trend for granite. The location of common and clay minerals in A-CN-K and A-CNK-FM space are plotted for comparison. Ka = kaolinite; Chl = chlorite; Plag = plagioclase feldspar; Ksp = potassium(K) feldspar; Feld = feldspar; Ill = Illite; Bio = biotite; Cal = calcite.

$$K = K_2O/(Al_2O_3 + CaO^* + N_2O + K_2O). \quad (3)$$

In the above, $CaO^*$ refers to CaO associated with the silicate fraction only. A, CN and K represent the proportions of molecular $Al_2O_3$, CaO + $N_2O$, and $K_2O$, respectively. In A-CN-K space, the proportion of molecular $Al_2O_3$ (A) is called the chemical index of alteration (CIA). Values of CIA are only calculated for granite and granodiorite samples. The results are plotted on a ternary diagram in order to determine the degree of surface related weathering (Nesbitt & Young 1982). An increase in CIA is expected for weathered samples, while for a typical un-weathered granitic rock, the CIA should be about 0.5. The majority of the samples plot on the join between plagioclase and K-feldspar (Fig. 10a), which is consistent with little to no alteration of feldspars to secondary clay, a characteristic reaction during the weathering process. In other words, the samples do not follow the theoretical compositional changes seen during progressive weathering for granites (Nesbitt *et al.* 1996). The only exceptions are samples taken from adjacent to secondary fault zones (Fig. 8b), where there is enrichment in Ca in the granodiorite, which is interpreted as the result of calcite metasomatism. This enrichment is manifested as calcite precipitation in voids, which means that $CaO^*$ does not represent the original igneous composition, and this in turn affects the CIA calculations.

A similar analysis was done using the Fe and Mg oxides (FM), this time lumping molecular CaO, $N_2O$ and $K_2O$ into one category (CNK). On an A-CNK-FM diagram, the core samples plot about the feldspar-biotite join (except for gouge samples), again indicating little or no weathering (Fig. 10b).

#### *4.2.2 XRD Mineralogy*

We analysed 62 of the core samples for clay mineralogy. Four representative diffractograms are shown in Fig. 11, for samples from the surface and from the core. All of the diffractograms for core samples, regardless of depth or type, contain chlorite (14.25, 7 and 4.8 Å). It is possible that the peak at 7 Å represents kaolinite as well, being that both kaolinite and Fe-rich chlorite collapse when heated to 550° (Martin 1955). All of the granite samples contain illite (characteristic peaks at 10.1 and 5 Å), although it could possibly be a mica, for instance muscovite, which was observed in thin sections. The typical smectite diffractogram (an indication of clay weathering) is recognized by the expansion of smectite upon glycolation and a shift of its 15 Å peak to around 17 Å, accompanied by the appearance of small peaks at 8.7 and 5.6 Å. When the sample is heated to 550°, the peak at 17 Å shifts to 9.9 Å. The presence of a hidden chlorite peak, revealed by the collapse of the smectite at 550° may point to a mixed-layer of chlorite-smectite (C-S). Smectite or C-S is the predominant clay mineral in the surface samples taken from the adjacent outcrop (e.g. sample DO13 in Fig. 11), similar to previous findings of weathering products in surface samples (Stillings 2007; Rockwell *et al.* 2009). Conversely, granitic core samples contain very little to no detectable smectite, even at shallow depths (e.g. sample LR04 in Fig. 11) with chlorite and illite as the predominant clay minerals, while the predominant clay in granodiorite and diorite samples is smectite/C-S at all depths (e.g. sample LR45 in Fig. 11). A noted exception in the granitic samples is demonstrated by LR30, which is located right above a secondary fault gouge layer, and its diffractogram clearly shows the presence of smectite (Fig. 11). This was observed for several granitic samples that are very close to gouge zones. The predominant clay minerals in the gouge samples are smectite and chlorite, and they contain a small quantity of illite. A small (yet consistent in all measurements) peak at 6.4 Å in the granitic samples probably indicates the presence of zeolites. Overall, evidence of surface weathering (as indicated by the presence of expandable clays, that is, smectite/C-S) below the surface is minor to absent in granite, and its presence in the other rock types at all depths is most likely composition related rather than a result of surface weathering.

## 5 DISCUSSION

### 5.1 PSD and *D*-values

Our particle size analyses for the pulverized granitoids at Littlerock are in good agreement with analyses of the Tejon Lookout Granite reported by Rockwell *et al*. (2009), in that the particles span a broad range of sizes and are mostly fine sand and silt in size, rather than following a narrow distribution with very fine particles as described by Wilson *et al*. (2005). We did not observe a difference in mineral composition between size fractions.

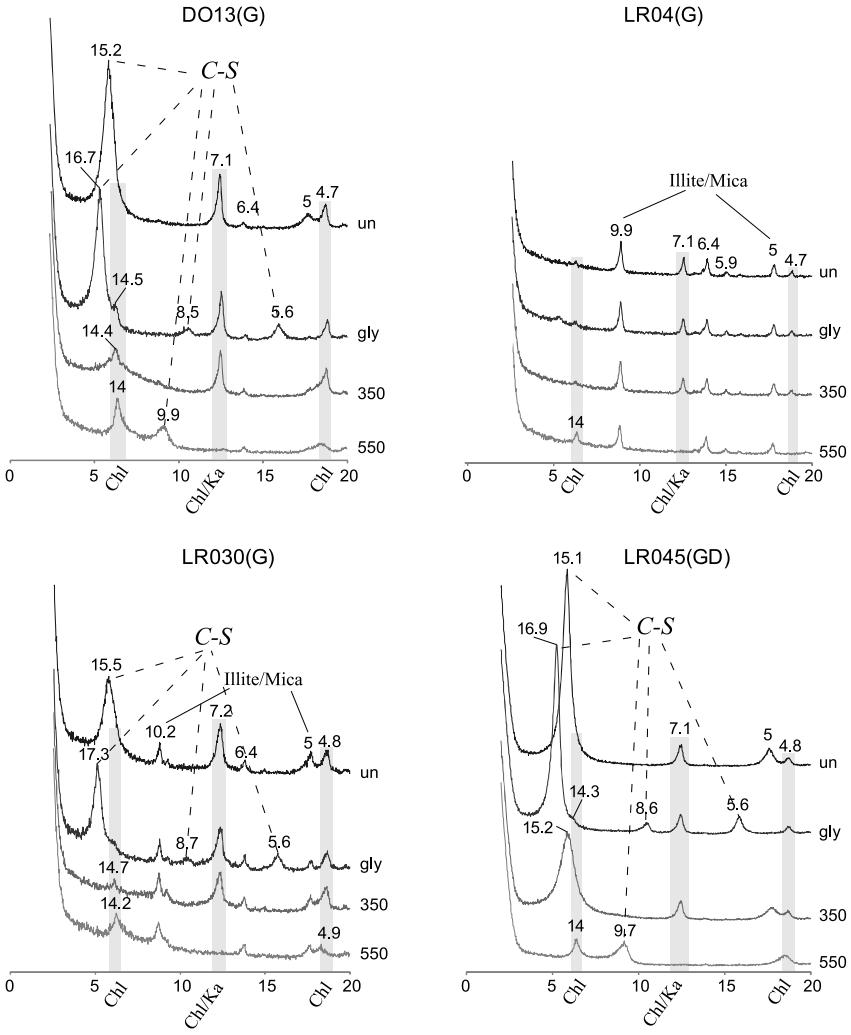


**Figure 11.** XRD diffractograms of four samples. DO13 is granitic surface sample from an outcrop next to the core location. It contains expandable clays (Smectite/Chlorite-Smectite). LR04 is granite from 2.3 m depth. It contains Chlorite and Illite (possibly mica), but almost no expandable clays. LR30 is granite from above a secondary fault gouge zone at 11.1 m depth. This sample is the only measured granitic core sample to contain a significant amount of expandable clays. LR45 is granodiorite from 19.1 m depth, and is a characteristic example of all the granodioritic samples from the core, containing expandable clays. For each sample 4 measurements are shown—the untreated sample (un), after glycolation (gly), after heating to 350° (350) and after heating to 550° (550). Spacing for each peak (in Å) is marked above. Ka, Kaolinite; Chl, Chlorite; C-S, Smectite or Chlorite-Smectite mixed layer.

Rockwell *et al*. (2009) noted that the PSD of pulverized Tejon Lookout Granite is not linear on a log–log plot of number versus size, and therefore does not define a true fractal population. The curvature of the PSD changes as a function of distance from the fault. The PSD curve of samples close to the fault displayed much more curvature than those farther from the fault, and the Tejon Pass sample at 20 m from the fault could be fitted equally well by a linear or a curved distribution. They used the following "power-log" function to fit their data:

$$y = ax^{(b \log x + c)}, \tag{4}$$

where $y$ represents the log of particle volumetric density, $x$ is the log of the particle diameter, and $a$, $b$ and $c$ are constants. The value of $b$ represents the curvature of the distribution, with $b = 0$ giving a straight (power-law) line. Rockwell *et al*. (2009) did not use a laser particle analyser for the Tejon pass samples, so a direct comparison to the core samples is not possible, but by rebinning the core PSD data into phi-scale it is possible to compare our results to theirs.

The PSD of samples at Littlerock, collected at about 80 m from the principal slip zone, follow a power-law distribution between 0.5 and 500 $\mu$m, with a $D$-value of 2.5–3.1. By re-binning and fitting the power-log function of eq. (4) between 0.5 and 4096 $\mu$m (–1 to 12 on phi scale), we examine whether our samples follow the same trend observed by Rockwell *et al*. (2009), namely that samples with a larger degree of damage are more curved. We cannot use the distance from the fault as a comparison parameter, and therefore we examine the changes in $b$ as a function of mean particle size and $D$-value (Fig. 12). The core samples mostly follow a similar trend to that observed by Rockwell *et al.* with decreasing curvature ($b$ closer to zero) correlated with smaller particles and higher $D$-values, except for the finest samples. Samples with $D$-values larger than 2.85 follow a reversed trend of decreasing curvature with increasing $D$-value, and their correlation with mean particle size does not hold. This reversed trend can introduce ambiguity of representation when using the power-log function and we therefore offer an alternative representation below.

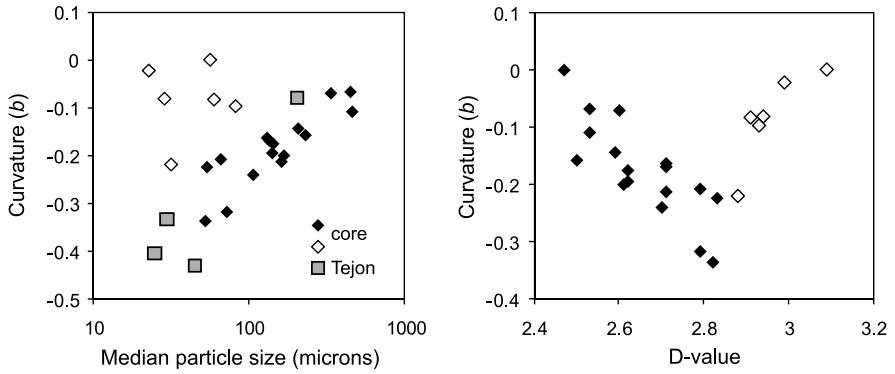


**Figure 12.** PSD curvature, represented by $b$ (see eq. 4), versus median particle size and $D$-value. Core samples are represented by diamonds; open diamonds represent the finest samples that do not follow the trend of decreasing curvature with decreasing particle size. Samples from the Tejon outcrop are represented by grey rectangles. Data for Tejon samples was taken from Rockwell *et al*. (2009).

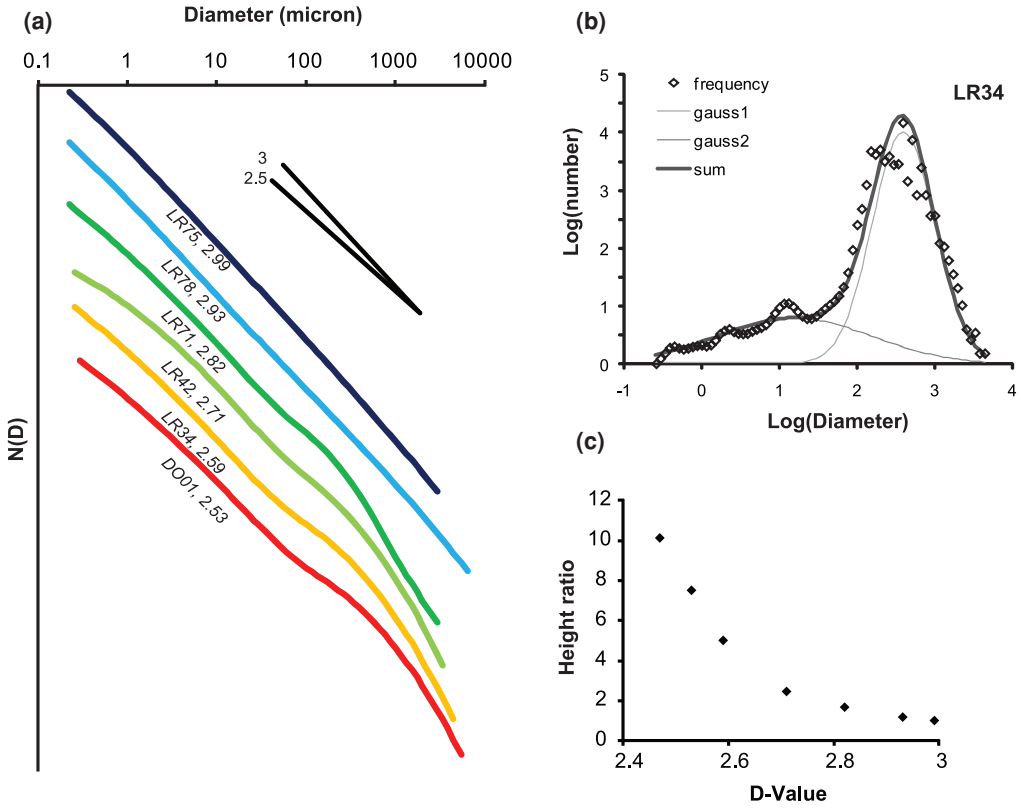


**Figure 13.** (a) PSD on a log–log plot for samples with different $D$-values. The numbers below the curves denote the D-values calculated for each sample as demonstrated in Fig. 6. (b) An example of fitting the sum of two Gaussians to sample's PSD (eq. 5). (c) Height ratio (eq. 7) versus $D$-value for the same samples as in (a).

It is possible to reasonably fit any of our PSD curves with a curve of the following form (a sum of 2 Gaussian distributions) on a log–log plot:

$$N(D) = a_1 \cdot \frac{1}{\sqrt{2\pi}\sigma_1} e^{-\frac{(D-\mu_1)^2}{2\sigma_1^2}} + a_2 \cdot \frac{1}{\sqrt{2\pi}\sigma_2} e^{-\frac{(D-\mu_2)^2}{2\sigma_2^2}}, \quad (5)$$

where $N(D)$ is log(volumetric percentage of particles), $D$ is log(diameter), $a_1$ and $a_2$ are coefficients, $\mu_i$ is the mean and $\sigma_i$ is the variance of each Gaussian distribution. By analyzing the data in this fashion, each PSD can be represented as two populations with normal distribution, one coarser with a mean log (diameter) (in $\mu$m) of 2.5–3, and one finer with a mean log (diameter) of 0.4–1. If the coarser population is more dominant (is the larger fraction), the PSD will appear more curved on a log–log plot and the $D$-value will be lower. If the finer population is more dominant, the PSD will be straight and the $D$-value higher. We demonstrate this idea for a subset of samples in Fig. 13(a), with an example of PSD curve fitting using eq. (5) in Fig. 13(b).

We can also examine the relative weight of the coarse and fine fractions. The height of each Gaussian distribution can be represented as

$$h_i = a_i/\sigma_i, \quad (6)$$

and the ratio between the coarse and fine Gaussian distributions needed to reconstruct the PSD would be

$$\text{height ratio} = \frac{h_{\text{coarse}}}{h_{\text{fine}}}. \quad (7)$$

This ratio is large when the coarse population is dominant and small when the fine population is dominant, and it is correlated to the *D*-value (Fig. 13c). This correlation does not reverse in the finest samples, in contrast to the power-log function used by Rockwell *et al*. (2009). When calculating the *D*-value over a smaller range, the larger particles, which behave in a non-power-law fashion, are omitted. The Gaussian representation is based on the entire particle size range.

It was suggested by various authors (e.g. Ann & Sammis 1994; Blenkinsop 1991; Chester *et al.* 2004; Keulen *et al.* 2007; Sammis & King 2007) that the *D*-values represent different mechanisms of grain size reduction, where values around 2.6 are characteristic of constrained comminution, that is, the condition where particle movement is constrained by neighbouring particles and high pressure, and the likelihood of particle fracture depends on the size of the particle and of neighbouring particles (Sammis *et al.* 1987). Values on the order of 3, often observed in gouge and foliated cataclasites, are thought to indicate comminution during cataclastic flow with significant displacement of particles by shear, and size reduction through fracture and abrasion processes (e.g. Keulen *et al.* 2007). Our samples do not cluster around either of those values, but rather span the range of 2.5–3.1. Moreover, our ability to represent successfully the observed PSD of various samples as a superposition of two Gaussians raises doubts on the validity of the common assumption that particles in pulverized rocks follow a fractal (scale-invariant) distribution.

The core taken at Littlerock is cut by numerous secondary faults, expressed as gouge zones, which likely also occur in the surface outcrops but are sometimes difficult to distinguish due to surface weathering. Combining the observation of secondary faulting with microstructural observations of pulverization and shear in thin sections (Fig. 3) and the variability in the *D*-values, we hypothesize that the PSD of core samples from Littlerock was produced by more than one mechanism. Likely mechanisms include shattering and grain size reduction by fracture and constrained comminution, possibly through dynamic changes of normal stress, as well as additional fracture and attrition associated with localized shear along secondary faults. These suggestions will be discussed further in a follow-up paper in which the mechanisms of fragmentation are investigated through detailed microscopic analysis of cored samples.

In terms of earthquake energy budget, our PSD results indicate that the damage is not homogeneous in its intensity, even in a single location (the core, in this case), and the distribution of particle sizes vary considerably within short distances of metres or less. We calculated a fracture surface area of $2.06 \times 10^8$ and $2.18 \times 10^8$ m$^2$ per cubic metre of pulverized material for the minimum and maximum *D*-values, respectively. This estimate from the core provides a point measurement in space relative to distance from the SAF. A comparison to the PF can be done using Chester *et al*. (2005) parameters ($d_{\min} = 3.2$ nm, $d_{\max} = 200$ $\mu$m, $D = 3$) and calculating fracture surface area per cubic metre in the same method as described in Section 3.3. Using those parameters, we obtain a value of $1.51 \times 10^9$ m$^2$ per cubic metre for the PF gouge (in the fault-core). Taking into account the finest particles, the fracture surface area calculated based on the PSDs at Littlerock is an order of magnitude smaller than estimates based on microfractures reported by Chester *et al*. (2005) for the PF-core. This estimate does not consider healed or sealed fractures, which are prevalent in the feldspar grains of some samples (e.g. see Fig. 3a). Pulverized rocks are part of the damage zone surrounding the fault-core, therefore it is not surprising that most of the fracture energy seems to be expended within the fault-core (gouge zone), compared with the surrounding damage zone.

### 5.2 Whole rock chemistry

The changes in bulk rock composition in the granites are compatible with the presence of authigenic calcite filling veins, as observed in thin sections. The reason for the mobility of Ca in the rock is possibly the albitization of plagioclase, which frees Ca ions from the lattice. The free Ca is then transported by fluids, possibly of meteoric origin, and is precipitated in cracks and voids. In the granodiorite, Ca enrichment occurs in the vicinity of shear and gouge zones (Fig. 8). Interestingly, granitic samples that were taken adjacent to shear zones in the core have a lower (<45 per cent) CIA than those taken away from shear zones, but are more similar in their major elements composition to the granite sample collected from a distant, non pulverized surface outcrop (Fig. 14). In contrast, the minor element compositions of all of the core granitic samples are similar (Fig. 14), but different in composition from the outcrop sample, probably because of fault related alterations that have changed the rock chemistry. The difference in the major-element composition between the granites within the core may reflect a fluid-assisted

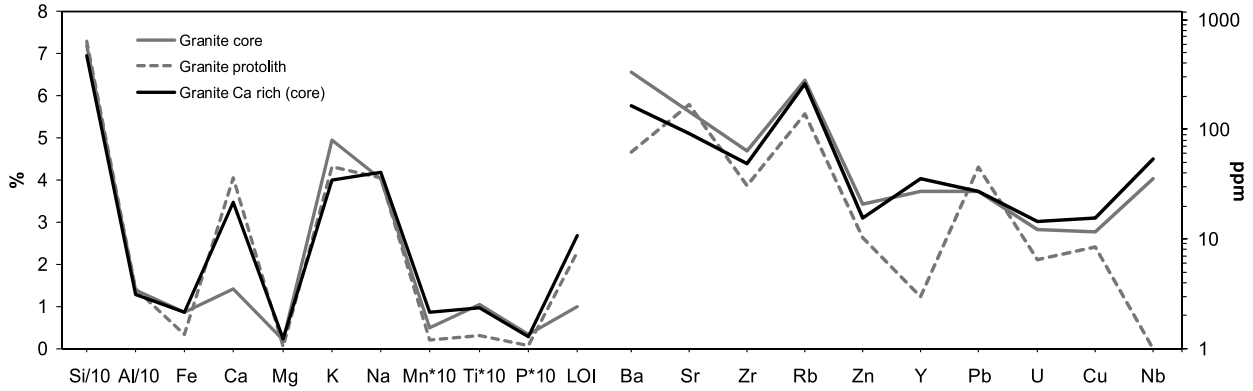


**Figure 14.** Comparisons of major and trace elements for the average granitic core samples, the protolith sample (Granite protolith), and the subset of low (>45 per cent) CIA granitic core samples next to secondary faults (Granite Ca rich).

enrichment of Ca along secondary faults which would lower the CIA and raise the Ca content with very little or no additional compositional changes. This assertion is supported by the similar LOI values between the two core sample groups, compared with the outcrop sample.

In general, fault zones consist of two parts; fine-grained fault gouge where slip occurs, and the surrounding damage zone where intact rocks are pervasively fractured (Caine *et al.* 1996) or pulverized (Dor *et al.* 2006). The fine grain gouge acts as a fluid barrier while the damage zone acts as a conduit; the fluids in turn can interact with the rock and change its composition. Fluid rock interaction at the Punchbowl and San Gabriel faults has been observed by various authors (Chester *et al*. 1993; Evans & Chester 1995), whereas others found very little evidence for it (Anderson *et al*. 1983). As observed in thin sections, some plagioclase is altered to laumontite, and there is also XRD evidence for laumontite presence in some samples. Laumontite can be formed by the albitization of plagioclase, and so could be a source of Ca for the calcite vein-fill. The rest of the changes in major element compositions are smaller than data variability and can be disregarded. The CIA presents additional support for fluid–rock interaction along faults, as it deviates from unaltered values (0.5) next to gouge/shear zones.

The major- and minor-element composition of the gouge samples is in between that of the granodiorite and the diorite compositions. This result suggests that the gouge was produced primarily by mechanical grinding of a mixture of the two host rocks, analogous to that found for the San Gabriel Fault (Evans & Chester 1995). There is, however, evidence for fluid-assisted chemical alteration within the gouge, such as the presence of smectite and kaolinite. Those two results are not contradictory if we assume that the fluid movement is restricted to gouge zones, so that the overall composition is unchanged.

### 5.3 Surface weathering

Although weathering was minor in the Tejon Lookout granites, Rockwell *et al*. (2009) did document the presence of pedogenic clays. Smectite and illite dominated the finest fraction of their samples, with the scattered occurrence of kaolinite. They concluded that these additional weathering products added to the cumulative weight of the finest materials measured, and therefore affected their PSD results. Rockwell *et al*. (2009) noted pedogenic clays were also observed in thin sections. In the Littlerock locality, we find similar evidence of pedogenic clays at the surface—smectite or C-S and possibly kaolinite. The presence of clay weathering products in the core samples is a function of their composition; however, the granitic samples from the surface did contain clay minerals associated with surface weathering while the core samples did not (Fig. 11). Therefore we conclude that the presence of smectite at depth is not necessarily a product of surface weathering. Rather, the assemblage smectite-chlorite (and possibly also illite) is thought to be the result of fluid–rock interaction and brittle deformation under low temperature conditions, as previously observed along exhumed traces of the SAF (Evans & Chester 1995). This conclusion is supported by the presence of smectite in granitic samples that are at close proximity to a fluid barrier such as a gouge layer, in contrast to its absence in all other measured granitic core samples. Schleicher *et al*. (2009) looked at the clay minerals in the SAFOD core and concluded that anomalously high illite-smectite and chlorite-smectite content correlated with the zones of active deformation. Our gouge samples from the core may be exhibiting the same behaviour, albeit with different protolith types (mudstone versus granite).

### 5.4 Chronology and mechanisms of damage

The above detailed observations raise the question of timing—when did each stage of deformation and alteration occur? There are no direct data as to the amount of exhumation at the Littlerock site, but data do exist for the San Gabriel Mountains south and west of Littlerock and the SAF. In the Mt. Baldy area, rocks are inferred to have been exhumed ∼3–5 km in the last 13 Myr, whereas in the western San Gabriel Mountains, the amount of exhumation is considerably less (Blythe *et al.* 2000). These estimates are for regions of high topography, so substantial past uplift is expected. In the vicinity of Littlerock, however, topography is generally low along the SAF so the amount of young exhumation is likely small. East of the fault, the Mojave block has sustained little or no exhumation since the Miocene, as there are Miocene sedimentary strata preserved (cf. Rainbow Basin) that have neither been greatly buried nor eroded. Considering that the Pliocene strata on each side of the fault (JHF on the west and Anaverde formation on the east) are similarly preserved, one can certainly make the argument that there has been no substantial exhumation since their deposition in the past few million years. Considering that the currently active strand of the SAF, adjacent to our study area, has been active since the Pliocene (Barrows *et al.* 1985), some of the healing and alterations observed in the rocks that are characteristic of higher temperatures (e.g. deeper) may be residuals from pre-SAF deformation at depth.

Wilson *et al*. (2003) inferred the relative timing of various deformation stages for the PF, and determined that microfracturing and healing occurred throughout the fault's activity, while other alterations were more confined in their timing. In thin sections, we see evidence of multiple cataclastic phases, where an earlier calcite-cemented cataclasite is broken again (e.g. Fig. 3c). There is also evidence for authigenic calcite deformation by twinning and cataclasis. Blenkinsop (1991) observed laumintitization along cracks and inferred chemically assisted fracturing. However, we do not see this in our samples, and the quartz is just as fractured as the altered plagioclase, without any obvious chemical processes assisting in its fracturing (Fig. 3a).

The core is cut by numerous shears that are obvious in hand sample and in thin section (Fig. 3f). The relative timing of shearing and pulverization is unknown. It is possible that the shears precede the microfracturing and the two damage textures represent two different phases of damage occurrence. It is also possible that they occur concurrently, and represent two different mechanisms of damage, but direct data to resolve the relative timing question was not observed.

Previous studies had documented pervasive granulation and pulverization of rocks away from the secondary faults and gouge zones over length scales of 100 m or more, combined with local preservation of the original appearance of the host rock (Wilson *et al.* 2005; Dor *et al.* 2006; Mitchell *et al.* 2011). These properties were used to distinguish pulverized rocks from more typical damage products and to point to a generation mechanism involving repeating episodes of dilation and contraction. In our study site, however, continuous pulverized zones sans shear are not common; in fact most of the cored interval was riddled with evidence for shear-related damage fabric in both the micro- and macroscales. As noted in Section 2.1, the study site may be part of a sliver of damaged rocks sandwiched between the SAF and PF. This may contribute to the mixture of damage products found in the core and enlarge the total amount of rock damage in the site.

The local zones of pulverization observed in this study and lack of significant weathering in these zones imply that the resulting

granulation has a mechanical origin that is distinct from the usual shear and attrition generally associated with fault zone damage. Given the close spatial association of the pulverized rocks with the active trace of the SAF in the Mojave (Dor *et al*. 2006), and the required high strain rates for pulverization (Doan & Gary 2009), the dilation and contraction episodes are most likely dynamic and produced by earthquake ruptures. The lack of abundant grains approaching the nano scale outside of gouge zones indicates that the pulverization does not necessitate an unusual shock-like stress loading (Sammis & Ben-Zion 2008). Previous authors suggested that the most likely generation mechanism for pulverized rocks is repeating occurrences of bimaterial ruptures producing strong dynamic reduction of normal stress near the propagating rupture front (Ben-Zion & Shi 2005; Dor *et al.* 2006; Mitchell *et al.* 2011). This was based on observed pulverized rocks belts (in the Mojave and other locations) associated with near-vertical strike-slip faults that separate different rock bodies, coupled with asymmetric damage distribution across these faults, with more damage on the side with higher seismic velocity at depth (Lewis *et al.* 2005; Dor *et al.* 2006; Dor *et al.* 2008, Wechsler *et al.* 2009). Given the single site scale of our study, we cannot add to the macroscopic observations of the above studies other than to note the complexity in our study area.

## 6 CONCLUSIONS

This paper describes pulverized fault zone rocks recovered from a shallow core along the SAF near Littlerock, with the primary goal of distinguishing the surface-weathering signal from damage reflecting fault zone processes.

At this site, the changes in bulk rock composition with depth suggest that some element transfer has resulted from fluid–rock interaction along secondary faults. XRD results indicate the existence of some surface weathering and the production of additional minor amounts of clay along secondary faults, which is apparently not related to surface weathering processes. Alteration and mineral growth are noted in thin section, as well as microfracture healing, although those can reflect healing of cracks that formed during cooling of the pluton or during unloading-exhumation.

The PSD is coarser and broader than previously determined by Wilson *et al*. (2005), and is similar overall to the results reported by Rockwell *et al*. (2009). The PSD follows approximately a power law relation but can also be fitted as a superposition of two Gaussians and perhaps other functional forms. Regardless of the precise form of the underlying distribution, the observations support the conclusion that the part of the total earthquake energy budget expended for breaking or shattering rocks is small to negligible.

An important observation is that the pulverized zone at Littlerock is cut by a multitude of secondary faults that are obvious at the mesoscopic and microscopic scales. This complexity may result in part from the location of the site. Most pulverized rock bodies in the Mojave are exposed north of the SAF and some of those show more continuous pulverization on the mesoscale. However, detailed analysis of the type done in this work may reveal complexity at the microscale also at such sites.

The relationship between the pulverization, shearing and their proximity to secondary faults makes the mechanisms of damage in the study site unclear. The observed *D*-values, which range between 2.5 and 3.1, are consistent with mixed populations of damage products in each sample. From qualitative analysis of thin sections, we suggest that the smaller particle sizes reflect comminution by shear, whereas the larger particles reflect the pulverization process.

The location of drill site is well within the fault damage zone, but our observations represent only one point in space. More work is needed in order to study the three-dimensionality of the damage zone in detail, and determine its effective width with respect to fluid–rock interactions and the spatial distribution of damage. Our observations support previous inferences on mechanical origin of the observed pulverized rocks, possibly related to the dynamic stress field generated by bimaterial ruptures, but many uncertainties remain. It is important to constrain further the origin of pulverization, and implications to earthquake and fault dynamics, by additional systematic observations in the structures of other faults (some clearly without bimaterial interface), along with additional laboratory and theoretical studies.

## ACKNOWLEDGMENTS

The authors wish to thank Joan Kimbrough for all her help in the SDSU chemistry lab, and to the SDSU geology students, especially Katie Anderson, for help in the lab and field. Thanks are also due to Professor R. W. Berry from SDSU for reviewing our clay mineralogy interpretations. The manuscript benefited from constructive comments by Diane Moore, Andrea Billi and an anonymous reviewer. This work was partially funded by the National Science Foundation Grant EAR-0510892 to JSC, and by the Southern California Earthquake Center (funded by NSF Cooperative Agreement EAR-0529922 and USGS Cooperative Agreement 07HQAG0008). The SCEC contribution number for this paper is 1458.

## REFERENCES

Anderson, J.L., Osborne, R.H. & Palmer, D.F., 1980. Petrogenesis of cataclastic rocks within the San Andreas fault zone of Southern California, U.S.A, *Tectonophysics,* **67**, 221–249.

Anderson, J.L., Osborne, R.H. & Palmer, D.F., 1983. Cataclastic rocks of the San Gabriel fault An expression of deformation at deeper crustal levels in the San Andreas fault zone, *Tectonophysics,* **98**, 209–251.

Ann, L.J. & Sammis, C.G., 1994. Particle size distribution of cataclastic fault materials from southern California—a 3-D study, *Pure appl. Geophys.,* **143**, 203–227.

Barrows, A.G., Kahle, J.E. & Beeby, D.J., 1985. *Earthquake Hazard and Tectonic History of the San Andreas Fault Zone,* Los Angeles County, CA.

Ben-Zion, Y., 2001. Dynamic ruptures in recent models of earthquake faults, *J. Mech. Phys. Solids,* **49**, 2209–2244.

Ben-Zion, Y., 2003. Appendix 2, Key Formulas in Earthquake Seismology, in *International Handbook of Earthquake and Engineering Seismology*, *Part B*, pp. 1857–1875, eds Lee, W.H.K., Kanamori, H., Jennings, P.C. & Kisslinger, C., Academic Press, Boston, MA.

Ben-Zion, Y. & Andrews, D.J., 1998. Properties and implications of dynamic rupture along a material interface, *Bull. seism. Soc. Am.,* **88**, 1085–1094.

Ben-Zion, Y. & Huang, Y., 2002. Dynamic rupture on an interface between a compliant fault zone layer and a stiffer surrounding solid, *J. geophys. Res.,* **107**, 2042, doi:10.1029/2001JB000254.

Ben-Zion, Y. & Shi, Z.Q., 2005. Dynamic rupture on a material interface with spontaneous generation of plastic strain in the bulk, *Earth planet. Sci. Lett.,* **236**, 486–496.

Blenkinsop, T.G., 1991. Cataclasis and processes of particle size reduction, *Pure appl. Geophys.,* **136**, 59–86.

Blythe, A.E., Burbank, D.W., Farley, K.A. & Fielding, E.J., 2000. Structural and topographic evolution of the central Transverse Ranges, California, from apatite fission-track, (U-Th)/He and digital elevation model analyses, *Basin Res.,* **12**, 97–114.

Brietzke, G.B., Cochard, A. & Igel, H., 2009. Importance of bimaterial interfaces for earthquake dynamics and strong ground motion, *Geophys. J. Int.,* **178**, 921–938.

Brune, J.N., 2001. Fault-normal dynamic unloading and loading: an explanation for "non-gouge" rock powder and the lack of fault-parallel shear bands along the San Andreas Fault, *EOS, Trans. Am. geophys. Un.,* **82**, 47.

Brune, J.N., Brown, S. & Johnson, P.A., 1993. Rupture mechanism and interface separation in foam rubber model of earthquakes: a possible solution to the heat flow paradox and the paradox of large overthrusts, *Tectonophysics,* **218**, 59–67.

Caine, J.S., Evans, J.P. & Forster, C.B., 1996. Fault zone architecture and permeability structure, *Geology,* **24**, 1025–1028.

Chester, F.M., Evans, J.P. & Biegel, R.L., 1993. Internal structure and weakening mechanisms of the San-Andreas Fault, *J. geophys. Res.,* **98**, 771–786.

Chester, F.M., Chester, J.S., Kirschner, D.L., Schultz, S.E. & Evans, J.P., 2004. Structure of large-displacement, strike-slip fault zones in the brittle continental crust, in *Rheology and Deformation in the Lithosphere at Continental Margins,* pp. 223–260, eds Karner, G. D., Taylor, B., Driscoll, N. W. & Kohlstedt, D. L. Columbia University Press, New York, NY.

Chester, J.S., Chester, F.M. & Kronenberg, A.K., 2005. Fracture surface energy of the Punchbowl fault, San Andreas system, *Nature,* **437**, 133–136.

Dalguer, L.A. & Day, S.M., 2009. Asymmetric rupture of large aspect-ratio faults at bimaterial interface in 3D, *Geophys. Res. Lett.,* **36**.

Doan, M.L. & Gary, G., 2009. Rock pulverization at high strain rate near the San Andreas fault, *Nat. Geosci.,* **2**, 709–712.

Dor, O., Ben-Zion, Y., Rockwell, T.K. & Brune, J., 2006. Pulverized rocks in the Mojave section of the San Andreas Fault Zone, *Earth planet. Sci. Lett.,* **245**, 642–654.

Dor, O., Yildirim, C., Rockwell, T.K., Ben-Zion, Y., Emre, O., Sisk, M. & Duman, T. Y., 2008. Geologic and geomorphologic asymmetry across the rupture zones of the 1943 and 1944 earthquakes on the North Anatolian Fault: possible signals for preferred earthquake propagation direction, *Geophys. J. Int.,* **173**, 483–504, doi:10.1111/j.1365–246X.2008.03709.x.

Evans, J.P. & Chester, F.M., 1995. Fluid-rock interaction in faults of the san-andreas system—inferences from San-Gabriel Fault rock geochemistry and microstructures, *J. geophys. Res.,* **100**, 13007–13020.

Flinn, D., 1977. Transcurrent faults and associated cataclasis in Shetland, *J. Geol. Soc. Lond.,* **133**, 231–248.

Girty, G.H. *et al*., 2006. Geology of Picacho State Recreation Area, SE California: Implications for the timing of the formation of the Chocolate Mountains anticlinorium, in *Using Stratigraphy, Sedimentology, and Geochemistry to Unravel the Geologic History of the Southwestern Cordillera: A Volume in Honor of Patrick L. Abbott,* pp. 77–96, eds Girty, G. H. & Cooper, J., Pacific Section SEPM book #101.

Girty, G.H., Biggs, M.A. & Berry, R.W., 2008. An unusual occurrence of probable Pleistocene corestone within a Cretaceous dioritic enclave, Peninsular Ranges, California, *Catena,* **74**, 43–57.

Keulen, N., Heilbronner, R., Stunitz, H., Boullier, A.M. & Ito, H., 2007. Grain size distributions of fault rocks: a comparison between experimentally and naturally deformed granitoids, *J. Struct. Geol.,* **29**, 1282–1300.

Lewis, M. A., Peng, Z., Ben-Zion, Y. & Vernon, F.L., 2005. Shallow seismic trapping structure in the San Jacinto fault zone near Anza, California, *Geophys. J. Int.,* **162**, 867–881.

Martin, R. T., 1955. Reference chlorite characterization for chlorite identification in soil clays, *Clays Clay Mineralogy,* NAS:NRC publication **395**, 117–145.

Mitchell, T. M., Ben-Zion, Y. & Shimamoto, T., 2011. Pulverized Fault Rocks and damage asymmetry along the Arima-Takatsuki Tectonic Line, Japan, *Earth planet. Sci. Lett.,* doi:10.1016/j.epsl.2011.04.023.

Nesbitt, H.W. & Young, G.M., 1982. Early Proterozoic climates and plate motions inferred from major element chemistry of lutites, *Nature,* **299**, 715–717.

Nesbitt, H.W., Young, G.M., McLennan, S.M. & Keays, R.R., 1996. Effects of Chemical weathering and sorting on the petrogenesis of siliciclastic sediments, with implications for provenance studies, *J. Geol.,* **104**, 525–542.

Rockwell, T.K., 2000. Use of soil geomorphology in fault studies, in *Quaternary Geochronology: Methods and Applications,* pp. 273–292, eds Noller, J. S., Sowes, J. M. & Lettis, W. R. American Geophysical Union, Washington, DC.

Rockwell, T.K., Sisk, M., Girty, G., Dor, O., Wechsler, N. & Ben-Zion, Y., 2009. Chemical and physical characteristics of pulverized Tejon Lookout Granite adjacent to the San Andreas and Garlock faults: implications for earthquake physics, *Pure appl. Geophys.,* **166**, 1725–1746.

Sammis, C.G. & Ben-Zion, Y., 2008. Mechanics of grain-size reduction in fault zones, *J. geophys. Res.,* **113**, B02306, doi:10.1029/2006JB004892

Sammis, C.G. & King, G.C.P., 2007. Mechanical origin of power law scaling in fault zone rock, *Geophys. Res. Lett.,* **34**.

Sammis, C.G., King, G. & Biegel, R., 1987. The kinematics of gouge deformation, *Pure appl. Geophys.,* **125**, 777–812.

Schleicher, A.M., Warr, L.N. & Van Der Pluijim, B.A., 2009. On the origin of mixed-layered clay minerals from the San Andreas Fault at 2.5–3 km vertical depth (SAFOD drillhole at Parkfield, California), *Contribut. Miner. Petrol.,* **157**, 173–187.

Sibson, R. H., 1986. Brecciation processes in fault zones: Inferences from earthquake rupturing, *Pure appl. Geophys.,* **124**, 159–176.

Shi, Z. & Y. Ben-Zion, 2006. Dynamic rupture on a bimaterial interface governed by slip-weakening friction, *Geophys. J. Int.,* **165**, 469–484, doi:10.1111/j.1365–246X.2006.02853.x.

Sperazza, M., Moore, J.N. & Hendrix, M.S., 2004. High-resolution particle size analysis of naturally occurring very fine-grained sediment through laser diffractometry, *J. Sediment. Res.,* **74**, 736–743.

Stillings, M.P., 2007. Structural, Textural, and geochemical analyses of fault damage zones: Clark Strand, San Jacinto Fault Zone, Southern California, *MSc thesis,* San Diego State University.

Wechsler, N., Rockwell, T.K. & Ben-Zion, Y., 2009. Application of high resolution DEM data to detect rock damage from geomorphic signals along the central San Jacinto Fault, *Geomorphology,* **113**, 82–96, doi:10.1016/j.geomorph.2009.06.007.

Wilson, B., Dewers, T., Reches, Z. & Brune, J.N., 2005. Particle size and energetics of gouge from earthquake rupture zones, *Nature,* **434**, 749–752.

Wilson, J.E., Chester, J.S. & Chester, F.M., 2003. Microfracture analysis of fault growth and wear processes, Punchbowl Fault, San Andreas system, California, *J. Struct. Geol.,* **25**, 1855–1873.

Zheng, G., Rice, J.R., 1998. Conditions under which velocity-weakening friction allows a self-healing versus a crack-like mode of rupture. *Bull. seism. Soc. Am.,* **88**, 1466–1483.

## APPENDIX A: PARTICLE SIZE DISTRIBUTION MEASUREMENT SCHEME

### A1. Sample preparation

Samples were gently disaggregated by hand before being run through a mechanical splitter. One split (about 40 gm each) was used for each PSD measurement. Sample splits were dried, weighed, and shaken in a horizontal box shaker for 24 hr with a dispersant (0.05N solution of sodium hexa-metaphosphate). Subsequently, samples were wet-sieved at either 63 or 125 $\mu$m (for pipette-sieve or automated method, respectively). The fine fraction was used for the standard pipette method and the Horiba laser particle analyses, and the coarse fraction was used for standard sieving and the Retch camsizer analyses. The coarse fractions were weighed, and then either dry-sieved using phi-interval sieves in order to combine the data with the pipette results, or run through the Retch camsizer and combined with the Horiba analyser results (by weight).

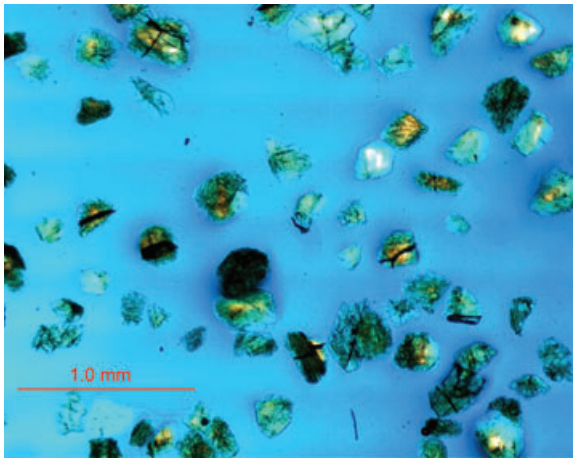


**Figure A1:** An example of a photomicrograph of grain mount used for calibration of the Horiba laser particle analyser, sample LR41. For each grain the maximum and minimum Feret diameters were recorded.

### A2. Automated method calibration

To calibrate the results from the Horiba analyser, we used the dry-sieved fractions of three previously measured (using pipette-sieve) samples (31–63, 63–125 and 125–250 $\mu$m). Each fraction was run in the Horiba analyser separately using several circulation speeds to produce a distribution. Additionally, grain mounts were made of each fraction and examined under light microscopy (Fig. A1). Using a microscope-mounted camera, we were able to measure the maximum and minimum Feret diameters (caliper widths) of 400 grains in each fraction. These data were used to calculate the PSD of each fraction. By comparing the microscopy and analyser results for a given fraction (Fig. A2), it was determined that the most consistent results are obtained using the measured minimum Feret diameter to calculate per cent by volume for the mounted samples. It is important to note, however, that the Horiba analyser consistently underestimated the particle size for the 125–250 $\mu$m fraction, shifting the PSD toward smaller values even when using various circulation speeds and analyser parameters. Therefore the upper size cut-off for the fine fraction (to be measured in the analyser) was determined to be 125 $\mu$m, even though the possible analyser measurement range stated by the manufacturer is up to 2 mm.

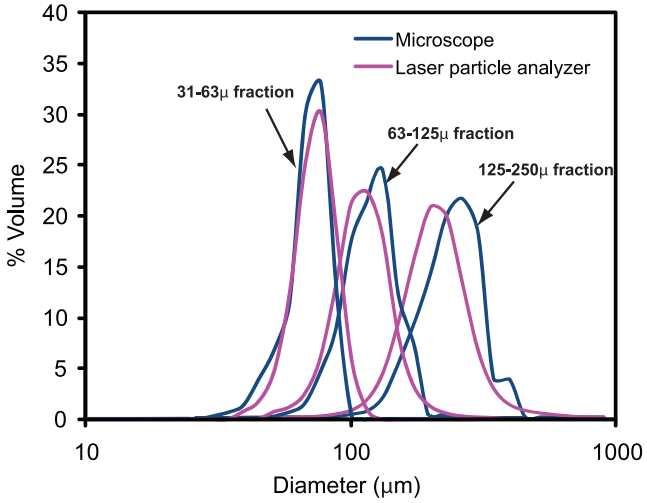


**Figure A2:** A comparison of microscope grain diameter measurements (minimum Feret diameter) with measurements of fractions in the Horiba analyser, for three fractions.

Using the calibration data, it is possible to make several observations regarding the performance of the Horiba analyser. First, the "tail" in the coarse fraction observed by Rockwell *et al*. (2009) is real, and is interpreted to be the result of the ellipsoid shape of some of the particles. A long and narrow fragment can pass through the sieve mesh in its narrow dimension during the shaking, yet the analyser might detect its larger dimension. For example, when observed under a microscope, the 125–250 $\mu$m fraction had grains with a maximum diameter of ∼400 $\mu$m and a minimum diameter of ∼90 $\mu$m. This produces 'tails' of particles that are larger or smaller than the sieve size. Our results indicate that the volumetric distribution calculated using the minimum Feret diameter was the most similar to the PSD produced by the Horiba analyser (Fig. A2).

We used our fraction calibration results to run 18 whole samples through the Horiba analyser and compare the results to the standard pipette-sieve method (Fig. 4). Each sample was run and measured at three circulation speeds (3, 4 and 5 in the Horiba analyser). Thus we determined which instrument parameters are the best for reproducing similar distributions. Parameters include circulation speed, percent of obscuration, index of refraction (Sperazza *et al*. 2004) and smoothness of distribution. The Horiba analyser has three index of refraction settings for grain shapes. The index of refraction that best reproduced the calibration measurements is that of non-circular, jagged quartz grains. The optimal per cent of obscuration, a measure of the amount of sample in the analyser's chamber, was between 15 and 25 per cent, similar to results by Sperazza *et al*. (2004). Following the result of the grain-mounting calibration, the minimum Feret diameter setting was used for the camsizer.

## SUPPORTING INFORMATION

Additional Supporting Information may be found in the online version of this article:

**Figure S1.** The complete log of the first Littlerock core (1.5–40.2 m depth), including lithology, shear zones and secondary fault locations and orientation (when available), sample names and locations, chemical index of alteration (CIA) and median grain size (in $\mu$m) for each sample.

**Figure S2.** The complete log of the second Littlerock core (35–42.7 m depth), including lithology, shear zones and secondary fault locations and orientation (when available), sample names and locations, chemical index of alteration (CIA) and median grain size (in $\mu$m) for each sample.

**Figure S3.** A photo-log of the cores, by depth (in feet). Depth increases from right to left. Scale is approximate due to difference in focal distances between the photos. Core sections are either 1 or 2 feet long. The fragility of the core prevented thorough cleaning and therefore some sections are partially covered by a 'crust' of oil (used for pipe lubrication).

**Table S1.** XRF major and trace elements data for surface and core samples, as well as CIA values, median grain size in $\mu$m, depth in metres, rock type (G-granite, GD-granodiorite, D-diorite) and *D*-value.

Please note: Wiley-Blackwell are not responsible for the content or functionality of any supporting materials supplied by the authors. Any queries (other than missing material) should be directed to the corresponding author for the article.